scientific reports

OPEN

Revisiting the far-field model of the force and torque induced on a conductive nonmagnetic sphere by a rotating magnetic dipole

Levi M. Barker[1]✉, Travis J. Allen[1,2], Adam J. Sperry[1,2] & Jake J. Abbott[1,2]✉

Time-varying magnetic fields generate eddy currents in an electrically conductive object, which then interact with the applied magnetic field, inducing force and torque on the object. This phenomenon has been used to perform dexterous noncontact manipulation of conductive nonmagnetic objects using multiple rotating magnetic dipole fields, utilizing an empirical model of the force-torque wrench induced by a rotating magnetic dipole field on a solid conductive sphere (which serves as an approximation for other geometries). In this study, we make two new contributions to the model. First, we gather data of the induced force-torque at a previously unconsidered configuration, which enables a complete characterization of the induced force-torque. Second, we identify a simplified model, valid at low rotation frequencies of the rotating magnetic dipole, that is substantially more intuitive, enabling new insight into how different independent parameters affect the induced force-torque. As with the prior model, our improved models are still far-field models, valid when two conditions are met: the magnetic dipole (which is assumed to be at the center of any physical field source) is at a distance from the surface of the conductive sphere that is at least as large as the sphere's diameter; and when the conductive sphere is outside of the minimum bounding sphere of the physical field source.

Time-varying magnetic fields generate eddy currents in electrically conductive objects[1], and when these eddy currents interact with the applied magnetic field, force and/or torque are induced on the conductive object. Existing applications of this phenomenon include, for example, material separation in metal recycling plants[2]. A rising area of interest for this phenomenon is in the remediation of space debris, as well as on-orbit servicing of satellites to prevent them from becoming debris[3–7]. These objects comprise large quantities of aluminum[8], which is electrically conductive but not ferromagnetic. Contactless manipulation has the benefit of reducing the chance of a destructive collision that could damage the object or create more space debris.

Our group has shown that the application of this phenomenon can be formulated as a robotic manipulation problem, where controlled manipulation in six degrees of freedom (6-DOF) is achievable using multiple field sources that generate rotating magnetic dipole fields[9–13]. This dexterous manipulation has been enabled by a model of the induced force-torque wrench on solid spheres formulated by Pham et al.[9], which can serve as a first-order approximation for other object geometries. That model only explicitly considered two canonical configurations of the sphere with respect to the rotating dipole field: on the axis of rotation of the rotating dipole; and in the plane swept by the rotating dipole, wherein the dipole is always orthogonal to the axis of rotation (Fig. 1). Later, Tabor et al.[12] showed that trigonometric functions can be used to interpolate the force-torque model from the canonical configurations to other configurations. However, it was discovered that additional data from a third, unmodeled, configuration was required to fully characterize the induced force-torque in arbitrary configurations; this was left as an open problem.

The model described above provides the foundation for manipulation algorithms developed to date, and enables feasibility studies in system design. As such, we would like the model to be as accurate and intuitive as possible. In this study, we make two new contributions to the model. First, we gather data of the induced force-torque on a solid conductive sphere at the aforementioned third configuration, using a new experimental apparatus, and the result is an improvement to the trigonometric interpolation of Tabor et al.[12] Second, we identify a simplified model, valid at relatively low (but still useful) rotation frequencies of the dipole, that is

[1]Department of Mechanical Engineering, University of Utah, Salt Lake City, UT, USA. [2]Robotics Center, University of Utah, Salt Lake City, UT, USA. ✉email: levi.barker@utah.edu; jake.abbott@utah.edu

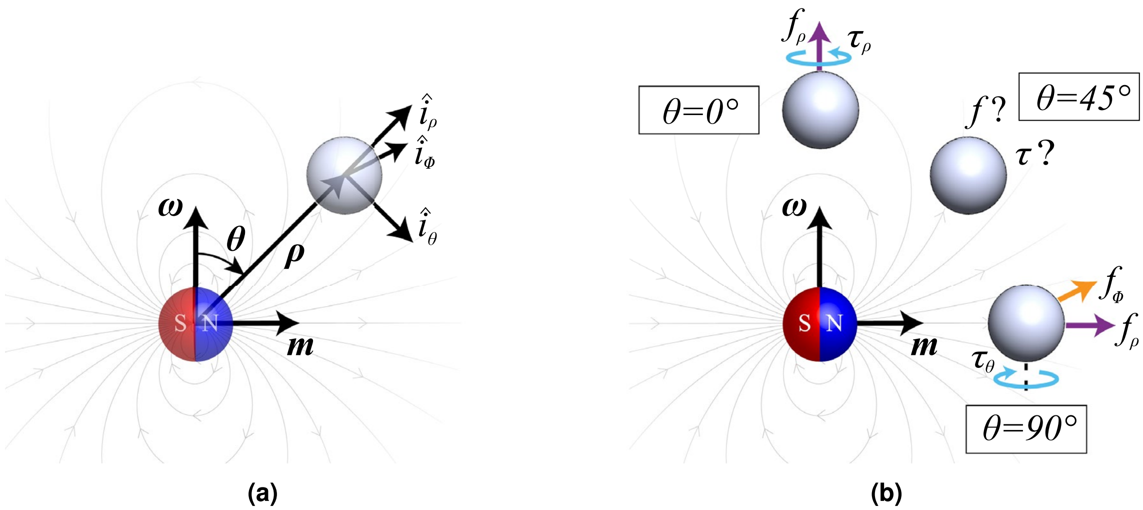

Fig. 1. Schematic of eddy-current-induced forces and torques on a conductive sphere. (**a**) Definition of the spherical coordinate system used to parameterize sphere location and force/torque vectors with respect to a rotating magnetic dipole. The magnetic dipole $\boldsymbol{m}$ and its field are depicted at a given instant, but are not relevant for the definition of the coordinate system. *Note*: $\hat{\boldsymbol{i}}_\phi$ points into the page. (**b**) Induced forces and torques at the previously modeled configurations $\theta = 0^\circ$ and $\theta = 90^\circ$ are shown. All force/torque arrowheads depict both the positive sign convention and the actual directions for the $\boldsymbol{\omega}$ shown. The previously unmodeled configuration at $\theta = 45^\circ$ is also shown.

substantially more intuitive, enabling new insight into how different independent parameters affect the induced force-torque.

Review of the existing model

Let us begin by summarizing the existing model, from Pham et al.[9], of induced force-torque on a solid conductive sphere due to a rotating magnetic dipole field. The magnetic dipole can be abstracted as a point dipole $\boldsymbol{m}$ at position $\mathscr{P}_{\boldsymbol{m}}$ rotating with angular velocity $\boldsymbol{\omega}$, such that $\boldsymbol{m}$ is orthogonal to $\boldsymbol{\omega}$(Fig. 1). We describe the position of the center of the conductive object as $\mathscr{P}_o$ and construct relative displacement vector $\boldsymbol{\rho} = \mathscr{P}_o - \mathscr{P}_{\boldsymbol{m}}$, described by three coordinates with respect to the rotating magnetic dipole: distance $\rho = \|\boldsymbol{\rho}\|$, polar angle θ measured from the dipole's rotation vector $\boldsymbol{\omega}$, and azimuthal angle ϕ measuring a right-handed rotation about $\boldsymbol{\omega}$. In this coordinate system, the previously modeled configurations are described by $\theta = 0^\circ$(and the symmetric $\theta = 180^\circ$) and $\theta = 90^\circ$. The force/torque vectors in this coordinate system can be decomposed into components in the directions of $\hat{i}_\rho$, $\hat{i}_\theta$, and $\hat{i}_\phi = \hat{i}_\rho \times \hat{i}_\theta$(which is undefined and unnecessary at $\theta = 0^\circ$ and $\theta = 180^\circ$).

The steady-state time-averaged induced force $\boldsymbol{f}$(units N) and torque $\boldsymbol{\tau}$(units N m) were modeled parametrically, at configurations $\theta = 0^\circ$ and $\theta = 90^\circ$, as a function of the radius r (units m) and electrical conductivity σ(units S $\mathrm{m}^{-1} = \mathrm{N}^{-1}{\cdot}\mathrm{m}^{-2}{\cdot}\mathrm{s\ A}^2$) of the conductive sphere, the distance ρ(units m) from the dipole (which is modeled as a point, which would be at the center of a physical source) to the center of the conductive sphere, the magnetic dipole strength $m = \|\boldsymbol{m}\|$(units A m^2), the dipole rotation frequency $\omega = \|\boldsymbol{\omega}\|$(units Hz), and the permeability of the environment μ(where $\mu_0 = 4\pi \times 10^{-7}$ N A^{-2}, the permeability of free space, is the only value of μ of any practical interest). Using the Buckingham Π theorem[14], the magnitude of each component of force and torque can be characterized using just two independent dimensionless Π groups, $\Pi_1 = \mu\sigma\omega r^2$ and $\Pi_2 = \rho r^{-1}$, where nondimensional force and torque, expressed by $\Pi_0 = f m^{-2}\mu^{-1}r^4$ and $\Pi_0 = \tau m^{-2}\mu^{-1}r^3$, respectively, are functions of Π_1 and Π_2.

It was observed that the far-field behavior, which was defined as $\Pi_2 > 1.5$(approximately), can be accurately described by a linear model of the form

$$\log_{10}(\Pi_0) = \xi \log_{10}(\Pi_2) + \psi \tag{1}$$

where $\xi = -7$ for components of force and $\xi = -6$ for components of torque—stemming from the form of the magnetic dipole field itself, rather than from the spherical object—with offset term ψ as some function of Π_1. After empirically fitting a function of the form

$$\psi = \log_{10}(c_0\Pi_1)c_1\Pi_1^{c_2} + c_3 \tag{2}$$

with component-specific coefficients c_0–c_3, the resulting dimensionless model for Π_0 took the form

$$\Pi_0 = (c_0\Pi_1)^{c_1\Pi_1^{c_2}}\,10^{c_3}\,\Pi_2{}^{\xi} \tag{3}$$

and the individual force/torque components are expressed by

$$f = 10^{c_3}\mu_0 m^2 \left(c_0\mu_0\sigma\omega r^2\right)^{c_1\left(\mu_0\sigma\omega r^2\right)^{c_2}} r^3\rho^{-7} \tag{4a}$$

$$\tau = 10^{c_3}\mu_0 m^2 \left(c_0\mu_0\sigma\omega r^2\right)^{c_1\left(\mu_0\sigma\omega r^2\right)^{c_2}} r^3\rho^{-6} \tag{4b}$$

These equations, although easily solvable numerically, are quite unintuitive, giving little insight into how forces and torques scale with respect to the size and conductivity of the sphere and the rotation frequency of the dipole.

Tabor et al.[12] showed that the force and torque at arbitrary values of ρ and θ, and not requiring ϕ due to symmetry, can be found using trigonometric-interpolation functions that call the model of (4) at the canonical configurations:

$$f_\rho(\rho,\,\theta) = \left(\frac{f_\rho(\rho,\,0^\circ) + f_\rho(\rho,\,90^\circ)}{2}\right) + \left(\frac{f_\rho(\rho,\,0^\circ) - f_\rho(\rho,\,90^\circ)}{2}\right)\cos(2\theta) \tag{5a}$$

$$f_\theta(\rho,\,\theta) = f_\theta(\rho,\,45^\circ)\sin(2\theta) \tag{5b}$$

$$f_\phi(\rho,\,\theta) = f_\phi(\rho,\,90^\circ)\sin(\theta) \tag{5c}$$

$$\tau_\rho(\rho,\,\theta) = \tau_\rho(\rho,\,0^\circ)\cos(\theta) \tag{5d}$$

$$\tau_\theta(\rho,\,\theta) = \tau_\theta(\rho,\,90^\circ)\sin(\theta) \tag{5e}$$

$$\tau_\phi(\rho,\,\theta) = 0 \tag{5f}$$

However, because the model for $f_\theta(\rho,\,\theta)$ requires knowledge of f_θ at $\theta = 45^\circ$, which was not available from Pham et al.[9], Tabor et al.[12] and all other subsequent works have simply assumed $f_\theta(\rho,\,\theta) = 0$, for lack of a better model. Our primary motivation for this study was to gather data, and find the coefficients c_0–c_3, at the third canonical configuration, $\theta = 45^\circ$. In the process, we also found a simpler and more-insightful model than (4), which is valid at low values of Π_1.

Results

Apparatus

Our experimental apparatus is shown in Fig. 2. We used a solid sphere of 2011-T3 aluminum with radius $r = 37.95$ mm and electrical conductivity $\sigma = 2.103 \times 10^7$ S m^{-1}. The force-torque induced on this sphere was measured using a 6-DOF force-torque sensor (ATI Nano17 Titanium with calibration SI–8–0.05), which collects data at a rate of 1 kHz. The sphere was rigidly mounted to the sensor with a 3D-printed adapter, which in turn is fixed to a support structure comprising nonconductive materials. Mounted to a 6-DOF robot arm (Universal Robots UR5e) is the end-effector developed by Allen et al.[13], which generates a time-varying magnetic field via rotation of a diametrically magnetized cylindrical permanent magnet with dipole-moment magnitude $m = 102.5$ A m^2.

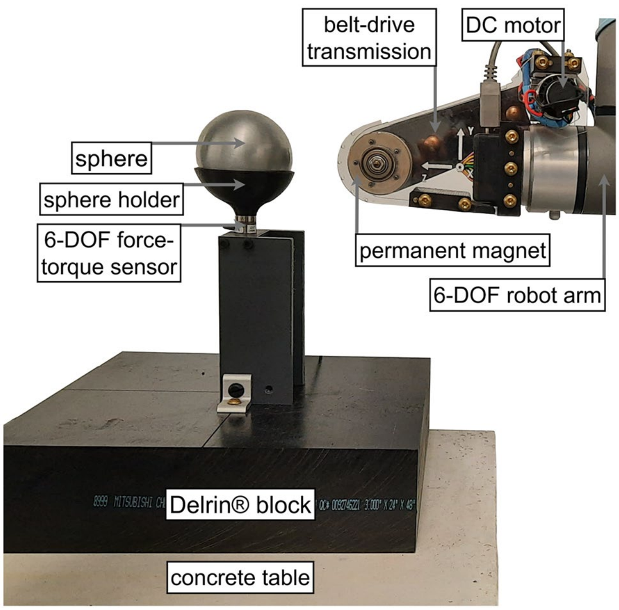

Fig. 2. Experimental apparatus, shown at $\theta = 90^\circ$, with $\boldsymbol{\omega}$ pointing out of the page.

Experimental parameters

In our study, we considered $\omega \in \{7.5, 15, 30, 60\}$ Hz. The upper rotation frequency was constrained by the maximum achievable by the experimental apparatus. The lower rotation frequency was chosen to ensure a sufficiently high signal-to-noise ratio in our force-torque measurements, based on pilot studies. We considered $\rho \in \{11, 12, 13, 14, 15\}$ cm. The farthest distance was chosen to ensure sufficiently high signal-to-noise ratios in our force-torque measurements, based on pilot studies. The nearest distance was chosen to ensure that the point dipole approximation was accurate, which for our cylindrical magnet is at distances ρ, measured from the center of the magnet, greater than 1.5 radii of the minimum bounding sphere of the magnet[15]. Given our fixed values of r, σ, and μ, this led to $\Pi_1 \in \{0.285, 0.571, 1.14, 2.28\}$ and $\Pi_2 \in \{2.90, 3.16, 3.42, 3.69, 3.95\}$. Experimental values of Π_0, for each component of force and torque, were collected at each combination of experimental parameters according to the procedure outlined in the Methods.

Elimination of outliers

A priori, we expected certain force/torque components to be zero due to symmetries: at $\theta = 0°$, these components are f_θ, f_ϕ, τ_θ, and τ_ϕ; at $\theta = 90°$, these components are f_θ, τ_ρ, and τ_ϕ. Using these known-zero components, we can quantify how sensor noise, in conjunction with the small imperfections in experimental configuration alignment, manifest in the resulting force/torque measurements. In Fig. 3a, we show experimental results for five trials at the closest experimental distance (*i.e.*, $\Pi_2 = 2.90$), which leads to the largest force and torque and thus the highest signal-to-noise ratio, for each experimental value of Π_1(*i.e.*, rotation frequency ω). For each trial, the measured force and torque vectors are first expressed in the spherical coordinate system by $\boldsymbol{f} = f_\rho \hat{\boldsymbol{i}}_\rho + f_\theta \hat{\boldsymbol{i}}_\theta + f_\phi \hat{\boldsymbol{i}}_\phi$ and $\boldsymbol{\tau} = \tau_\rho \hat{\boldsymbol{i}}_\rho + \tau_\theta \hat{\boldsymbol{i}}_\theta + \tau_\phi \hat{\boldsymbol{i}}_\phi$, respectively. We then calculate the angular error, γ, in the force/torque vector if we were to assume each component, one at a time, was identically equal to zero. We see that all the components we expected to be zero due to symmetries can, in fact, be set to zero with very little change in the estimated force/torque vector.

Using this process, the largest error experimentally observed was $\gamma = 1.2°$, which we used to establish a cutoff of $\gamma = 1.3°$, below which we would simply assume a component to be equal to zero. Using this cutoff, we consider the components at the configuration $\theta = 45°$ in Fig. 3b. τ_ϕ is likely identically equal to zero. f_θ is nonzero, but for small values of Π_1 represents a negligible contribution; such trials falling below the angle cutoff are omitted from the modeling process.

General model

In Figs. 4a, 5a, and 6a, we show experimental results at $\theta = 0°$, $\theta = 45°$, and $\theta = 90°$, respectively, in which the model (1) is fit, via the intercept term ψ, through the mean of the five trials for the parameter set with the smallest Π_2(*i.e.*, the closest location), which has the highest signal-to-noise ratio. We can see that this linear model (in log-log space) is a good predictor of Π_0 across all values of Π_2 tested, validating the original far-field model at the novel configuration of $\theta = 45°$. In Figs. 4b, 5b, and 6b, we show the respective resulting ψ values as a function of $\log_{10}(\Pi_1)$. We used least-squares regression to fit the nonlinear model of (2) to the data set, generating coefficients c_0–c_3 at each configuration. They are provided in Table 1. The high R^2_{adj} values indicate that the existing model of Pham et al.[9] is as good a fit at the novel configuration as it was at the original two. Over the domain considered here, the models for configurations $\theta = 0°$ and $\theta = 90°$ are comparable to

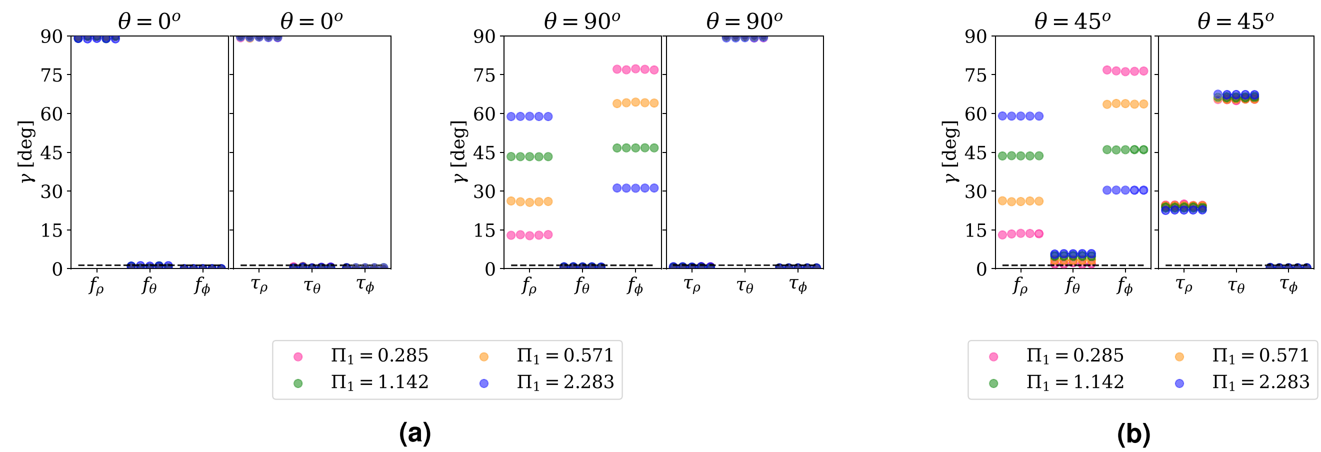

Fig. 3. Angular error, γ, in the estimated force/torque vector if a given component is assumed to be zero (one at a time), over five trials, at the closest distance (*i.e.*, $\Pi_2 = 2.90$) for each experimental value of Π_1. Configurations with components that were known to be zero *a priori* are shown in (**a**); these components motivated the 1.3° cutoff, indicated by the dashed black line, which was used to determine which components to model as equal to zero at the novel configuration shown in (**b**).

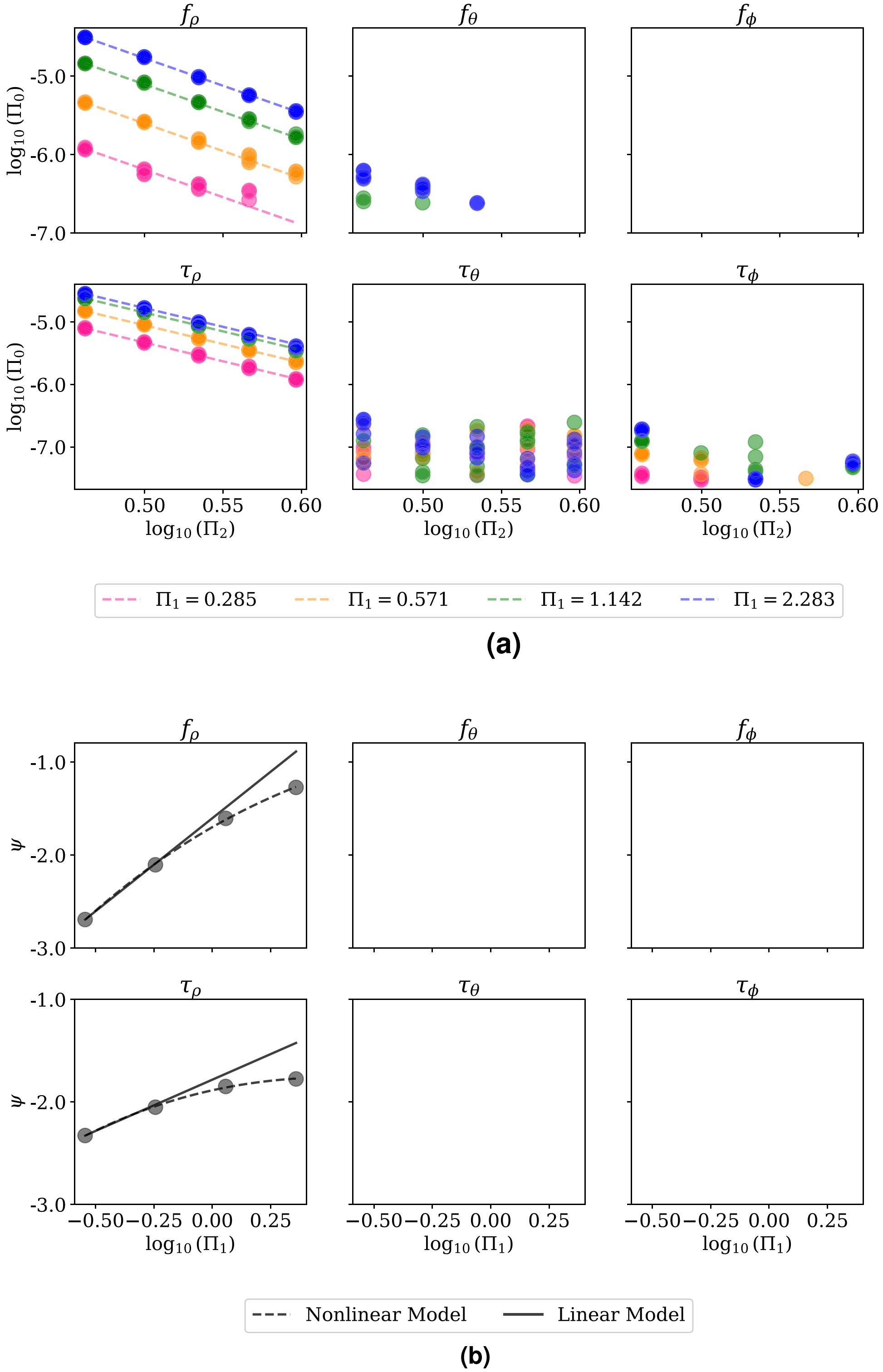

Fig. 4. Experimental results at $\theta = 0°$. Note that the four components without curves were already deemed zero-force/torque components.

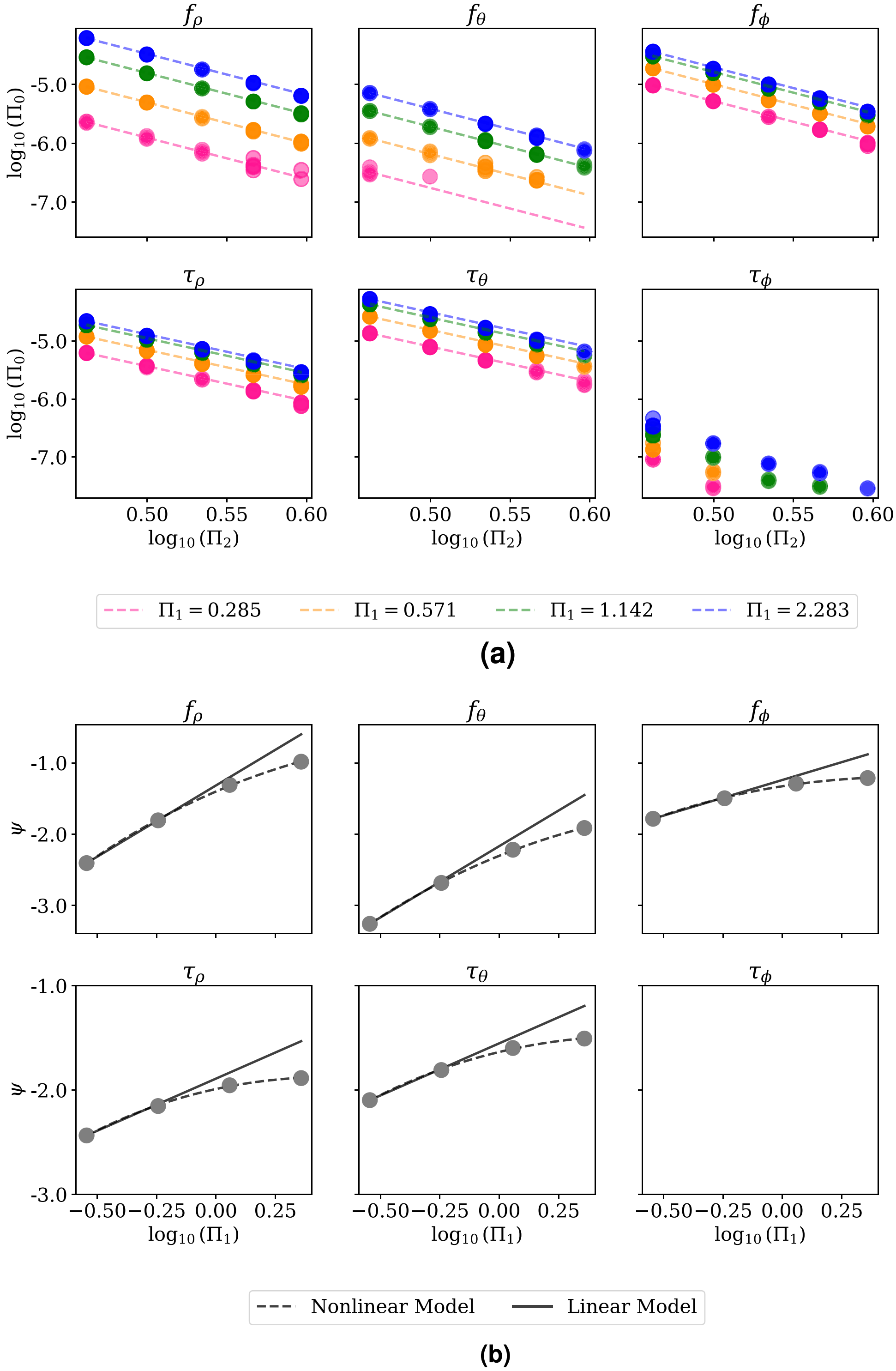

Fig. 5. Experimental results at $\theta = 45°$. Note that τ_ϕ was already deemed a zero-torque component.

those reported in Pham et al.[9], even though they were obtained with a different experimental apparatus (see Supplementary Materials).

Low-Π_1 model

After observing that, at relatively low values of the dipole rotation frequency ω, some force-torque components seem to be approximately linear with respect to ω, and some seem to be approximately quadratic with respect to ω, we verified that a linear model of the form

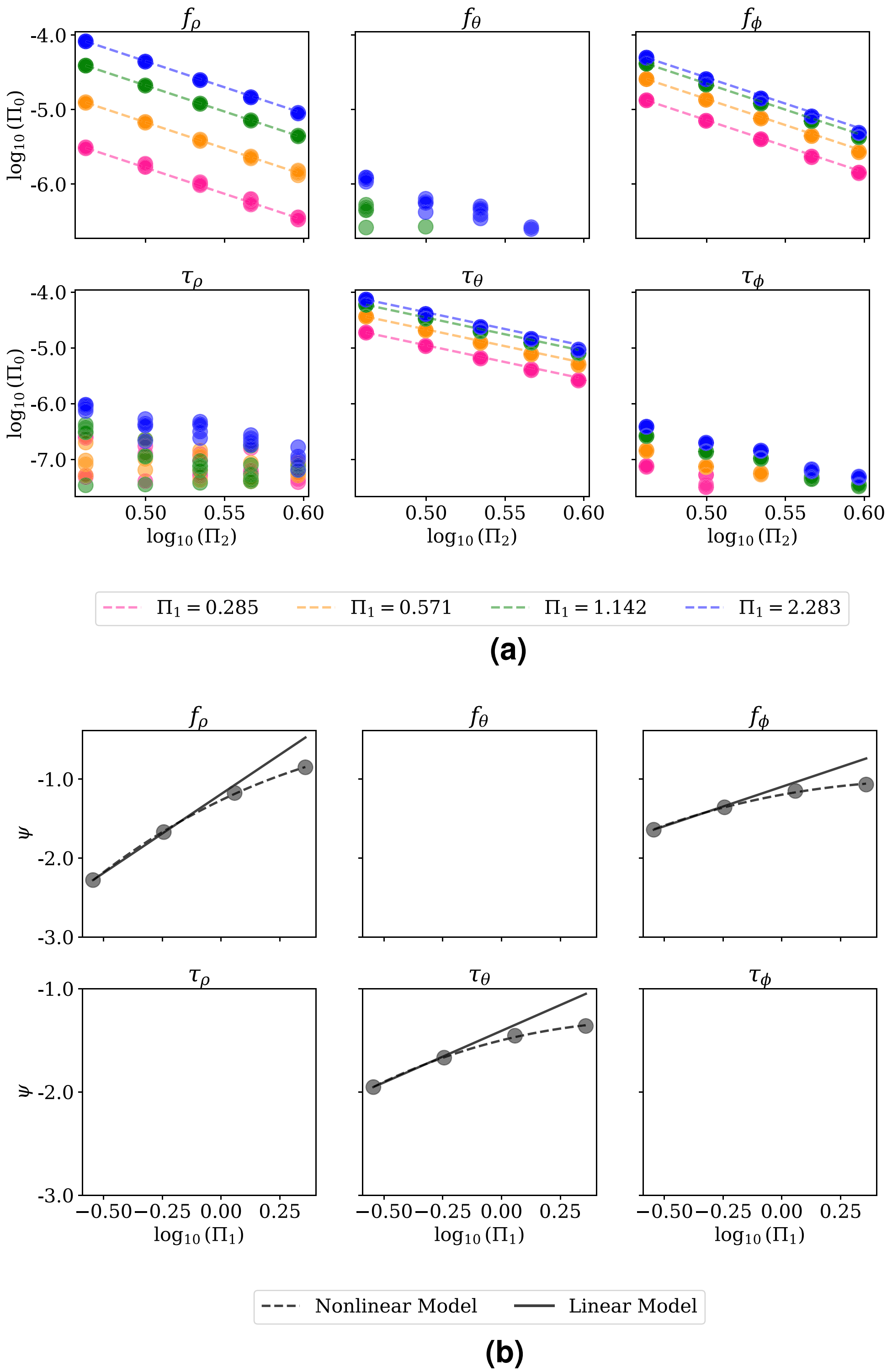

Fig. 6. Experimental results at $\theta = 90°$. Note that the three components without curves were already deemed zero-force/torque components.

$$\psi = \alpha \log_{10}(\Pi_1) + \beta \tag{6}$$

with $\alpha = 2$ for the f_ρ and f_θ components and $\alpha = 1$ for the remaining components, is a good fit to the data at low values of Π_1 at all three configurations tested. We fit this linear model through the value of ψ at the lowest value of Π_1 (*i.e.*, $\Pi_1 = 0.285$); the resulting coefficient β for each force/torque component is provided in Table 1. The resulting linear fits at at each configuration are shown in Figs. 4b, 5b, and 6b.

	ξ	Nonlinear model					Linear model	
		c_0	c_1	c_2	c_3	R^2_{adj}	α	β
Coefficients at $\theta = 0°$								
f_ρ	−7	430	4.04	−0.106	−12.3	1.00	2	−1.60
τ_ρ	−6	6840	4.16	−0.0996	−17.8	1.00	1	−1.78
Coefficients at $\theta = 45°$								
f_ρ	−7	348	4.15	−0.112	−11.9	1.00	2	−1.32
f_θ	−7	1680	4.95	−0.0981	−18.3	1.00	2	−2.17
f_ϕ	−7	3020	3.90	−0.108	−14.9	1.00	1	−1.24
τ_ρ	−6	3420	4.01	−0.108	−16.1	0.99	1	−1.89
τ_θ	−6	4050	3.83	−0.103	−15.5	0.99	1	−1.55
Coefficients at $\theta = 90°$								
f_ρ	−7	266	4.09	−0.117	−11.2	1.00	2	−1.19
f_ϕ	−7	6040	3.46	−0.0969	−14.3	0.99	1	−1.10
τ_θ	−6	8100	3.63	−0.0939	−15.7	0.99	1	−1.41

Table 1. Component-specific model coefficients at three configurations, for nonlinear and linear models of ψ, valid over the domain $\Pi_1 \in [0,\ 2.28]$ and $\Pi_2 > 1.5$.

Combining (1) and (6), we arrive at a model to describe Π_0 in terms of the two independent Π groups, applicable for low values of Π_1:

$$\Pi_0 = 10^\beta \Pi_1^\alpha \Pi_2^\xi \tag{7}$$

which, when expressed in terms of individual force/torque components, becomes

$$f_\rho = 10^\beta m^2 \mu_0^3 \sigma^2 \omega^2 r^7 \rho^{-7} \tag{8a}$$

$$f_\theta = -10^\beta m^2 \mu_0^3 \sigma^2 \omega^2 r^7 \rho^{-7} \tag{8b}$$

$$f_\phi = 10^\beta m^2 \mu_0^2 \sigma \omega r^5 \rho^{-7} \tag{8c}$$

$$\tau_\rho = 10^\beta m^2 \mu_0^2 \sigma \omega r^5 \rho^{-6} \tag{8d}$$

$$\tau_\theta = 10^\beta m^2 \mu_0^2 \sigma \omega r^5 \rho^{-6} \tag{8e}$$

$$\tau_\phi = 0 \tag{8f}$$

These equations can now be called by the trigonometric-interpolation functions in (5). Note that, since Π_0 should be interpreted as the magnitude of the force/torque component in question, the negative sign in (8b) was added manually to correctly capture the sign of the f_θ component in the spherical coordinate system when used in conjunction with (5b).

Figure 7 shows the error incurred by using the low-Π_1 model, calculated by

$$\text{Prediction Error } \% = \frac{\|\boldsymbol{f}_{\text{mod}} - \boldsymbol{f}_{\text{data}}\|}{\|\boldsymbol{f}_{\text{data}}\|} \times 100\%$$

where $\boldsymbol{f}_{\text{data}}$ represents the experimentally measured force vector and $\boldsymbol{f}_{\text{mod}}$ represents the force vector that is predicted by the low-Π_1 model at that Π_1 value. Errors in torque vectors are calculated analogously. We computed a force/torque error of approximately 5% at $\Pi_1 = 0.571$ and approximately 30% at $\Pi_1 = 1.14$. These errors are invariant to Π_2. As a rough guideline, we can say that low-Π_1 model is very accurate for $\Pi_1 < 0.5$, and quite inaccurate for $\Pi_1 > 1$.

Discussion

An examination of the low-Π_1 model—which, for a given conductive sphere with fixed radius and conductivity, can be thought of as a low-frequency model—reveals a few salient facts that provide substantially more intuition than did (4) about how force-torque scales with various independent parameters:

- All force/torque components are quadratically proportional to the dipole strength, *m*, as expected from the dimensional analysis. This is also true of the prior model.
- All force components decay with distance ρ(from the center of the dipole field source to the center of the conductive sphere) to the seventh power, and all torque components decay with distance to the sixth power, as

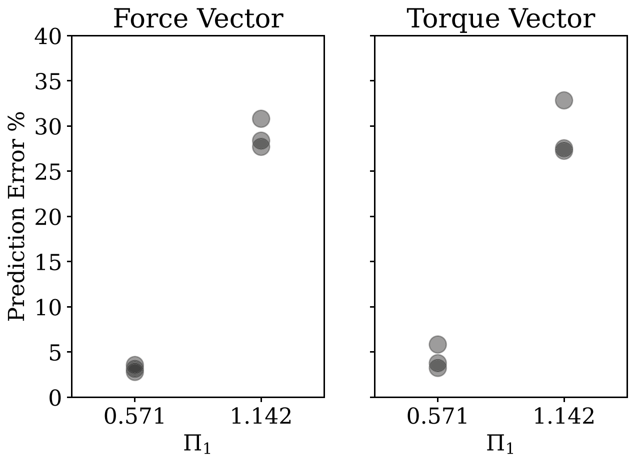

Fig. 7. The error incurred from using the low-Π_1 model to predict the induced force and torque vectors. Each data point corresponds to one of the three configurations tested.

hypothesized from an examination of the dipole-field model. This is also true of the prior model. As with the prior model, this should be assumed to be a far-field behavior, valid when $\rho > 1.5r$(approximately).

- Force components f_ρ and f_θ(*i.e.*, the force vector that lies in the plane spanned by vectors $\boldsymbol{\rho}$ and $\boldsymbol{\omega}$) are proportional to the conductive sphere's radius, *r*, to the seventh power. The remaining force component, f_ϕ, and all torque components, are proportional to the conductive sphere's radius, *r*, to the fifth power.
- The sphere's conductivity, σ, and the magnetic dipole's rotation frequency, ω, enter the equations for the force/torque components as a single product, $\sigma\omega$, as expected from the dimensional analysis. This means that the effect of an increase in σ is indistinguishable from the effect of an increase in ω by the same factor. This is also true of the prior model, although it has not been noted in prior works.
- Force components f_ρ and f_θ(*i.e.*, the force vector that lies in the plane spanned by vectors $\boldsymbol{\rho}$ and $\boldsymbol{\omega}$) are quadratically proportional to $\sigma\omega$, and cubically proportional to the permeability of the environment. The remaining force component, f_ϕ, and all torque components, are linearly proportional to $\sigma\omega$, and quadratically proportional to the permeability of the environment.
- It is a fortunate coincidence that when considering aluminum (the material of greatest use in engineered space objects) the conductivity, σ, is numerically comparable to the inverse of the permeability of free space, μ_0. The result is that the cubic effect of μ_0 and quadratic effect of σ in the force components f_ρ and f_θ has the same approximate combined effect as the quadratic effect of μ_0 and linear effect of σ in the remaining force/torque components. Thus, we may conceptualize all force/torque components as being quadratic with respect to μ_0 and linear with respect to σ, with f_ρ and f_θ as being quadratic with respect to ω, and the remaining force/torque components as being linear with respect to ω.
- For the force vector in the plane spanned by vectors $\boldsymbol{\rho}$ and $\boldsymbol{\omega}$, we find that f_θ is always smaller in magnitude than f_ρ, but is not always negligible as assumed in prior works. We find that f_θ makes its largest contribution to that vector at the (symmetric) angles of $\theta = 32^\circ$ and $\theta = 148^\circ$, where it represent 16.7% of the total force vector in that plane (see Supplementary Materials).
- For a sphere with density η, we can calculate its mass as $(4/3)\pi\eta r^3$ and moment of inertia as $(8/15)\pi\eta r^5$. If we fix the value of ω, and thus Π_1, to enforce the low-Π_1 model (*e.g.*, $\Pi_1 = 0.5$), the forces and torques in (8) can be expressed as translational and angular accelerations, respectively. We find that translational accelerations are invariant to the sphere's radius r, whereas angular accelerations are proportional to r^{-2}. Thus, for a given Π_1, smaller spheres are easier to angularly accelerate than larger spheres.

In a recent work from our group that considered the use of the same rotating permanent magnet used herein to despin the same aluminum sphere used herein (motivated by detumbling of uncooperative space objects)[13], it was found that there was a negligible benefit of increasing ω above 30 Hz, which corresponds to $\Pi_1 = 1.14$ and $\log_{10}(\Pi_1) = 0.058$. This is in agreement with the results of Figs. 4b, 5b, and 6b. Further, once we consider the practical hardware limitations in generating high ω, whether using a rotating permanent magnet or an electromagnetic field source (as we have done in most of our prior works on this topic), one may find that the simplicity of the low-Π_1 model justifies restricting ω to this regime.

Finally, we note that, although we consider our models to be valid in the far-field regime (*i.e.*, $\Pi_2 > 1.5$, approximately), due to the practical limitations in our experimental apparatus, we were not able to gather any experimental data in the near-field regime (*i.e.*, $\Pi_2 < 1.5$, approximately). Neither was Pham et al.[9] The existence of a near-field regime, in which the far-field model underpredicts the actual induced force and torque, is purely based on finite-element-analysis results from Pham et al.[9], and has yet to be verified experimentally. This remains an open problem.

Methods

For each combination of experimental parameters, the following procedure was performed.

1. The end-effector was placed by the robot at the pose specified by the trial's θ and Π_2 value, using the MoveIt 2 motion planner.
2. 6-DOF force-torque measurements were collected for 5 s while the end-effector's permanent magnet was held still; this data was time-averaged.
3. 6-DOF force-torque measurements were collected for 15 s while the permanent magnet accelerated to the ω specified by the trial's Π_1 value and then maintained under closed-loop control. The final 5 s of data, representing steady-state behavior, was time-averaged. The permanent magnet was then brought to rest.
4. Sensor bias was removed by subtracting the results of Step 2 from the results of Step 3. These results were then converted from the sensor's coordinate frame to the sphere's body-centered coordinate frame and then expressed in the spherical coordinate system of Fig. 1.
5. Steps 2 through 4 were repeated, for a total of five trials per parameter combination.

The results were used to compute the associated Π_0 for each component of force and torque. Any measurements below the published resolution of the sensor are omitted from the modeling process, as well as from any figures.

Data availability
All data generated or analyzed during this study are included in this published article (and its Supplementary information files).

Received: 10 February 2025; Accepted: 12 May 2025
Published online: 25 May 2025

References

1. Hertz, H. *Miscellaneous papers*, chap. II. On induction in rotating spheres (London: Macmillan, 1896). English translation by D. E. Jones and G. A. Schott.
2. Smith, Y. R., Nagel, J. R. & Rajamani, R. K. Eddy current separation for recovery of non-ferrous metallic particles: A comprehensive review. *Miner. Eng.* **133**, 149–159 (2019).
3. Sugai, F., Abiko, S., Tsujita, T., Jiang, X. & Uchiyama, M. Detumbling an uncontrolled satellite with contactless force by using an eddy current brake. In *Proceedings of the IEEE/RSJ International Conference on Intelligent Robots and Systems*, pp. 783–788 (2013).
4. Ortiz Gómez, N. & Walker, S. J. I. Eddy currents applied to de-tumbling of space debris: Analysis and validation of approximate proposed methods. *Acta Astronaut.* **114**, 34–53 (2015).
5. Youngquist, R. C., Nurge, M. A., Starr, S. O., Leve, F. A. & Peck, M. A slowly rotating hollow sphere in a magnetic field: First steps to de-spin a space object. *Am. J. Phys.* **84**, 181–191 (2016).
6. Nurge, M. A., Youngquist, R. C., Caracciolo, R. A., Peck, M. & Leve, F. A. A thick-walled sphere rotating in a uniform magnetic field: The next step to de-spin a space object. *Am. J. Phys.* **85**, 596–610 (2017).
7. Liu, X., Lu, Y., Zhou, Y. & Yin, Y. Prospects of using a permanent magnetic end effector to despin and detumble an uncooperative target. *Adv. Space Res.* **61**, 2147–2158 (2018).
8. Opiela, J. N. A study of the material density distribution of space debris. *Adv. Space Res.* **43**, 1058–1064 (2009).
9. Pham, L. N. et al. Dexterous magnetic manipulation of conductive non-magnetic objects. *Nature* **598**, 439–443 (2021).
10. Dalton, D. K., Tabor, G. F., Hermans, T. & Abbott, J. J. Attracting conductive nonmagnetic objects with rotating magnetic dipole fields. *IEEE Robot. Autom. Lett.* **7**, 11484–11491 (2022).
11. Dalton, D. K., Tabor, G. F., Hermans, T. & Abbott, J. J. Position regulation of a conductive nonmagnetic object with two stationary rotating-magnetic-dipole field sources. *IEEE Trans. Robot.* **40**, 4635–4647 (2024).
12. Tabor, G. F., Pham, L. N., Abbott, J. J. & Hermans, T. Magnetic manipulation of unknown and complex conductive nonmagnetic objects with application in the remediation of space debris. *Int. J. Robot. Res.* https://doi.org/10.1177/0278364924130016 (2024).
13. Allen, T. J., Sperry, A. J., Posselli, N. R., Minor, B. A. & Abbott, J. J. Characterization of a rotating magnetic dipole field for contactless detumbling of space debris. In *Proceedings of an International Conference on Space Robotics*, pp. 119–124 (2024).
14. Buckingham, E. On physically similar systems; illustrations of the use of dimensional equations. *Phys. Rev.* **4**, 345 (1914).
15. Petruska, A. J. & Abbott, J. J. Optimal permanent-magnet geometries for dipole field approximation. *IEEE Trans. Magn.* **49**, 811–819 (2013).

Acknowledgements
This work was supported by National Science Foundation under Grant 2149585, and by the Air Force Research Laboratory, AFWERX, AFRL/RGKB under Contract Nos. FA9453-22-C-A044 and FA864923P1235, which is a collaboration with Rogue Space Systems.

Author contributions
J.J.A. motivated the research, and acquired funding. L.M.B. and J.J.A. designed the experiment. T.J.A., L.M.B., and A.J.S. developed the experimental apparatus and methodology. T.J.A. and L.M.B. conducted the experiments. L.M.B. conducted the data analysis, performed the model fitting, and drafted the manuscript. All authors reviewed and edited the manuscript.

Declarations

Competing interests
The authors declare no competing interests.

Additional information
Supplementary Information The online version contains supplementary material available at https://doi.org/10.1038/s41598-025-02214-5.

Correspondence and requests for materials should be addressed to L.M.B. or J.J.A.

Reprints and permissions information is available at www.nature.com/reprints.